International Journal of Heat and Mass Transfer 51 (2008) 5991–6005

Contents lists available at ScienceDirect

International Journal of Heat and Mass Transfer

journal homepage: www.elsevier.com/locate/ijhmt

Transient laminar opposing mixed convection in a differentially and asymmetrically heated vertical channel of finite length

L. Martínez-Suástegui [a,*], C. Treviño [b]

[a] Facultad de Ingeniería, Universidad Nacional Autónoma de México, C. U. México 04510 DF, Mexico
[b] Facultad de Ciencias, Universidad Nacional Autónoma de México, C. U. México 04510 DF, Mexico

ARTICLE INFO

Article history:
Received 29 October 2007
Received in revised form 12 April 2008
Available online 21 June 2008

Keywords:
Mixed convection
Opposed flows
Unsteady convective flows
Asymmetrical heating

ABSTRACT

Transient laminar mixed convection in an asymmetrically and differentially heated vertical channel of finite length subject to an opposing buoyancy is investigated by solving the unsteady two-dimensional Navier–Stokes and energy equations. Results illustrate the effects of buoyancy strength or Richardson number $Ri = Gr/Re^2$ and Reynolds number Re on the overall flow structure and the nondimensional heat flux (Nusselt number) from the heated surface. Final steady or oscillatory flow response is obtained depending on the value of the Reynolds and Richardson numbers. The critical value of the buoyancy strength between the two regimes strongly depends on the value of the Reynolds number.

1. Introduction

Buoyant effects in fluid flow in channels have been studied extensively due to its practical applications including the design of compact heat exchangers, solar collectors, nuclear reactors and the cooling of electronic equipment. The subject of forced and mixed convection in rectangular ducts with uniform heating conditions has been widely treated in the literature, as can be seen in the review on this subject by Hartnett and Kostic [1]. The study by Aung and Worku [2] provided theoretical results for mixed convection flows between parallel plate channels with unequal wall temperatures and showed that when the parameter Gr/Re exceeds a certain threshold value, flow reversal occurs. In further studies for vertically upward flow in a parallel plate channel, the same authors [3] presented criteria for the occurrence of flow reversal and showed that buoyancy dramatically increases the hydrodynamic development length and diminishes the thermal development distance. Sparrow et al. [4] performed experiments that revealed the presence of a pocket of downflow and recirculation in a buoyancy-driven flow in a heated vertical channel, where one of the principal walls was maintained at a uniform temperature above that of the ambient, while the other principal wall was not heated. Elpidorou et al. [5] reported numerical results for two-dimensional, steady mixed convection from a flush-mounted, isoflux heat source on one side of a vertical channel with adiabatic walls, reporting the effect of opposite wall boundary conditions in the velocity and temperature fields. The unsteady laminar aiding and opposing mixed convection heat transfer in a vertical flat duct was numerically investigated for an initially fully developed flow by Lin et al. [6], obtaining correlation equations for the time variations of local Nusselt numbers with wall-to-fluid heat capacity ratios. In [7], Lin et al. numerically investigated the transient laminar opposing mixed convection in a vertical plane channel subject to a symmetric heat input, reporting periodic flow and thermal evolution in space and time along with detailed flow and thermal characteristics. Yao [8] obtained an analytical solution for the fluid flow and the heat transfer in the entry region of a heated vertical channel for constant wall temperature and constant wall heat flux conditions, suggesting that moving periodic and recirculating cells are generated if natural convection is a dominant mode. Chang and Lin [9] numerically investigated the buoyancy and inertia effects on a low Prandtl fluid flowing through a symmetrically and uniformly heated vertical plane channel subject to an opposing buoyancy, pointing out that an oscillatory flow with a single fundamental frequency is found when the buoyancy parameter or Richardson number, which is a function of the Reynolds number, exceeds a critical value. The linear stability of mixed convection in a differentially heated vertical channel for various Prandtl numbers was studied by Chen and Chung [10], indicating that the flow can become unstable under appropriate conditions. In [11], Cheng et al. made numerical predictions of buoyancy assisted flow reversal and convective heat transfer in the entrance region of a vertical rectangular duct, investigating cases with various

* Corresponding author. Present address: Department of Mechanical Engineering, University of California, Riverside, CA 92521, USA. Tel.: +1 951 827 2022; fax: +1 951 827 2829.
E-mail address: martinezlorenzo@gmail.com (L. Martínez-Suástegui).

0017-9310/$ - see front matter © 2008 Elsevier Ltd. All rights reserved.
doi:10.1016/j.ijheatmasstransfer.2008.04.055

Nomenclature

$2D$	bidimensional value
f	frequency (Hertz)
g	magnitude of the gravitational acceleration
Gr	Grashof number based on the channel width, $Gr = g\beta(T_w - T_0)h^3/\nu^2$
h	channel width (characteristic length)
J	heat transfer coefficient
L	nondimensional length of the channel, $L = L_1 + L_2 + L_3$
L_1^*	length from the channel inlet to the heated plate (see Fig. 1)
L_1	$L_1 = L_1^*/h$
L_2^*	length of the heated plate (see Fig. 1)
L_2	$L_2 = L_2^*/h$
L_3^*	length from the heated plate to the channel outlet (see Fig. 1)
L_3	$L_3 = L_3^*/h$
Nu	Nusselt number (see Eq. (13))
$\overline{Nu}$	average Nusselt number (see Eq. (13))
P	nondimensional pressure, $(p - p_0 - \rho_0 gx)/\rho_0 u_0^2$
Pe	Peclet number, $U_0 h/\alpha$
Pr	Prandtl number, ν/α
q	heat flux per unit area on the heated plate
Re	Reynolds number based on the channel width, $Re = u_0 h/\nu$
Ri	Richardson number based on the channel width, $Ri = Gr/Re^2$
St	Strouhal number, $St = fh/u_0$
t	time
T	temperature
T_0	fluid temperature at the channel inlet
T_w	temperature of the heated plate
U	u/u_0, longitudinal adimensional velocity
u_0	fluid velocity at the channel inlet
u, v	longitudinal and transversal velocity components, respectively
V	v/u_0, transversal adimensional velocity
x, y, z	Cartesian rectangular coordinates
X	adimensional longitudinal coordinate, $X = x/h$
Y	adimensional transverse coordinate, $Y = y/h$
Y_p	mass flux centroid, defined in Eq. (21)

Greek symbols

α	thermal diffusivity
β	thermal volumetric expansion coefficient
γ	heat loss parameter
λ	coefficient of thermal conductivity
μ	dynamic viscosity
ν	kinematic viscosity
ρ_0	density for $T = T_0$
ψ	adimensional stream function
ω	adimensional vorticity
θ	adimensional temperature
τ	adimensional time
ξ	function that generates the mesh in the longitudinal direction (see Eq. (17))
η	function that generates the mesh in the transverse direction (see Eq. (14))

Subscripts

i, j	space coordinates
cr	critical value
co	cutoff
o	atmospheric pressure

asymmetric heating conditions over wide ranges of parameters, finding that the strength and the extent of the reversed flow are dependent on the buoyancy parameter, the cross-sectional aspect ratio, and the Prandtl number. Evans and Greif [12] studied numerically the downward flow of nitrogen in a tall, partially heated vertical channel, showing the strong effects of buoyancy even for small temperature differences and reporting time dependant oscillations including periodic flow reversals along the channel walls. Numerical studies for mixed convection heat transfer and buoyancy-induced flow separations in a duct with complex geometry were made by Cheng et al. [13]. Jang and Yan [14] made a numerical study of mixed convection heat and mass transfer along a vertical wavy surface that is maintained at uniform temperature by using a coordinate transformation to transform the complex wavy surface to a flat plate, presenting developments of skin-friction coefficient, velocity, temperature, concentration, Nusselt number and Sherwood number along the wavy surface. El-Din [15] investigated the effect of thermal and mass buoyancy forces on the development of laminar mixed convection between two parallel plates with uniform heat and mass fluxes presenting velocity, temperature and concentration profiles and how they are affected by the Richardson number. Martínez-Suástegui and Treviño [16] carried out particle image velocimetry (PIV) measurements in an experimental investigation of laminar mixed convection in a vertical duct with a square cross section. In their experiments, the main downward water-flow is driven by gravity while a portion of a lateral side is heated, and buoyancy forces produce non-stationary vortex structures close to the heated region. In this study, the authors report that the vortex dimensions are independent of the channel depth. Therefore, although the studied instability in this numerical investigation is three-dimensional, it is valid to describe the problem with a two-dimensional model. Their results illustrate the influence of the Reynolds number and the Richardson number in the fluid flow structure and vortex sizes and locations, reporting that the flow patterns are nonsymmetric, periodic, and that they exhibit increasing complexity and frequency for increasing buoyancy.

Despite the extensive studies on steady mixed convection in vertical channels that have been carried out in the past, relatively little attention has been paid to investigating transient unstable thermal and flow characteristics in internal mixed convection flow with a flat velocity distribution at the channel entrance. The aim of this paper was to conduct a detailed numerical study of unsteady laminar mixed convection in a vertical plane channel for higher values of the Richardson number when the flow opposes buoyancy in order to unravel how the values of the Reynolds and Richardson numbers affect the overall flow and heat transfer characteristics.

2. Governing equations

Consider a Newtonian, two-dimensional, laminar downflow at the entrance of a vertical duct with x being the axial coordinate (positive downward) and y the transverse coordinate ($y = 0$ at the left wall). It is assumed that the flow is driven by gravitational forces acting vertically downward. The forced flow at the inlet section of the duct is at ambient temperature T_0 and has a uniform velocity u_0 with a flat distribution. On the left wall there is a discrete heat source of length L_2^*, located at $x = L_1^*$, with uniform wall temperature T_w, where $T_w > T_0$. All other channel walls are

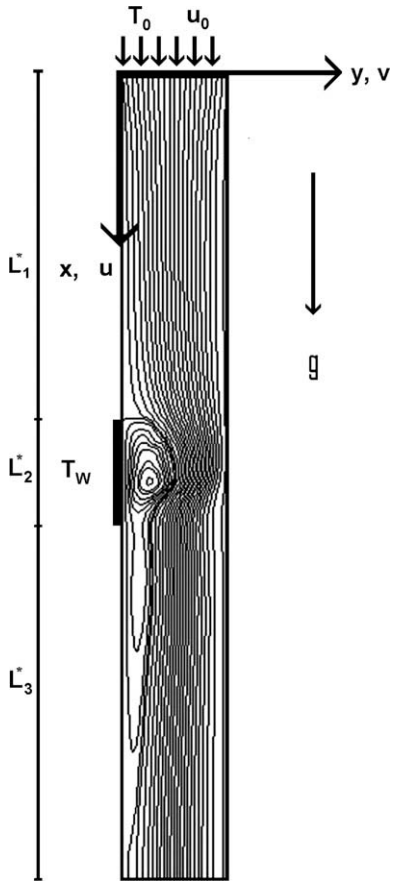

Fig. 1. Schematic diagram of the flow and heat transfer problem.

assumed to have heat transfer losses, which are linearly related to the temperature difference with the ambient temperature. The effect of viscous dissipation is neglected and the fluid properties are assumed constant except for the variation of density in the buoyancy term of the longitudinal momentum equation (Boussinesq approximation). The geometry under investigation is shown in Fig. 1. It is to be noticed that flow rectifiers are placed at both ends, channel entrance and exit, thus producing a parallel flow at $x = 0$ and $x = L_1^* + L_2^* + L_3^*$. It is also assumed that as the fluid leaves the channel, there is no more influence to the flow inside the channel. This can be obtained by including a short receptacle to collect the outgoing fluid followed by an open exit to the atmosphere.

The basic equations that govern the two-dimensional flow and heat transfer, in nondimensional form are given by

$$\frac{\partial U}{\partial X}+\frac{\partial V}{\partial Y}=0 \tag{1}$$

$$\frac{\partial U}{\partial \tau}+U\frac{\partial U}{\partial X}+V\frac{\partial U}{\partial Y}=-\frac{\partial P}{\partial X}+\frac{1}{Re}\left(\frac{\partial^2 U}{\partial X^2}+\frac{\partial^2 U}{\partial Y^2}\right)+H(\tau)Ri\theta \tag{2}$$

$$\frac{\partial V}{\partial \tau}+U\frac{\partial V}{\partial X}+V\frac{\partial V}{\partial Y}=-\frac{\partial P}{\partial Y}+\frac{1}{Re}\left(\frac{\partial^2 V}{\partial X^2}+\frac{\partial^2 V}{\partial Y^2}\right) \tag{3}$$

$$\frac{\partial \theta}{\partial \tau}+U\frac{\partial \theta}{\partial X}+V\frac{\partial \theta}{\partial Y}=\frac{1}{Pe}\left(\frac{\partial^2 \theta}{\partial X^2}+\frac{\partial^2 \theta}{\partial Y^2}\right) \tag{4}$$

In the above equations, all velocity components are scaled with the inflow velocity, u_0, $U = u/u_0$ and $V = v/u_0$; the longitudinal coordinates are scaled with the channel width h, $X = x/h$ and $Y = y/h$; the time is scaled with the residence time h/u_0, $\tau = tu_0/h$; the temperature is normalized as $\theta = (T - T_0)/(T_w - T_0)$, and the relative pressure is scaled with the dynamic pressure, $\rho_0 u_0^2$, $P = (p - p_0 - \rho_0 gx)/\rho_0 u_0^2$. Re is the Reynolds number, $Re = u_0 h/\nu$, Pr is the Prandtl number, $Pr = \nu/\alpha$, and $Pe = PrRe$ is the Peclet number. The Richardson number is defined as $Ri = Gr/Re^2$, where Gr is the Grashof number, $Gr = g\beta(T_w - T_0)h^3/\nu^2$. Here $H(\tau)$ corresponds to the Heaviside step function. Eqs. (1)–(4) are to be solved with the following boundary conditions:

$$\begin{aligned}
&U = V = \frac{\partial P}{\partial Y}-\frac{1}{Re}\frac{\partial^2 V}{\partial Y^2}=0 \quad \text{at } Y=0,1\\
&P = U-1 = V = 0, \quad \text{at } X=0\\
&\theta = 1 \quad \text{at } Y=0, \quad \text{for } L_1 \leqslant X \leqslant L_1+L_2\\
&\frac{\partial \theta}{\partial Y}=\gamma\theta \quad \text{at } Y=0, \quad \text{for } L_1 > X > L_1+L_2\\
&\frac{\partial \theta}{\partial Y}=-\gamma\theta \quad \text{at } Y=1\\
&\frac{\partial \theta}{\partial X}=V=\frac{\partial U}{\partial X}=0 \quad \text{at } X=L_1+L_2+L_3
\end{aligned} \tag{5}$$

Here γ corresponds to the heat loss parameter given by $\gamma = Jh/\lambda$, where J is the heat loss transfer coefficient and λ is the fluid thermal conductivity. The initial condition for the fluid flow corresponds to that without buoyancy, $U = U_p(X, Y)$, which results from a forced flow along the channel and is obtained from Eqs. (1)–(4) with $Ri = 0$. Except for a rapid unimportant transient at the beginning, this transient problem corresponds to that with a step change in the temperature at the heated slab from T_0 to T_w at time $t = 0$.

Using the vorticity ($\omega = \partial V/\partial X - \partial U/\partial Y$) and stream function ($U = \partial\psi/\partial Y$, $V = -\partial\psi/\partial X$) formulation, Eqs. (1)–(4) transform to

$$\frac{\partial^2 \psi}{\partial X^2}+\frac{\partial^2 \psi}{\partial Y^2}=-\omega \tag{6}$$

$$\frac{\partial \omega}{\partial \tau}+\frac{\partial \psi}{\partial Y}\frac{\partial \omega}{\partial X}-\frac{\partial \psi}{\partial X}\frac{\partial \omega}{\partial Y}=\frac{1}{Re}\left(\frac{\partial^2 \omega}{\partial X^2}+\frac{\partial^2 \omega}{\partial Y^2}\right)-H(\tau)Ri\frac{\partial \theta}{\partial Y} \tag{7}$$

$$\frac{\partial \theta}{\partial \tau}+\frac{\partial \psi}{\partial Y}\frac{\partial \theta}{\partial X}-\frac{\partial \psi}{\partial X}\frac{\partial \theta}{\partial Y}=\frac{1}{Pe}\left(\frac{\partial^2 \theta}{\partial X^2}+\frac{\partial^2 \theta}{\partial Y^2}\right) \tag{8}$$

subject to the following nondimensional boundary conditions:

$$\begin{aligned}
&\omega = \frac{\partial \psi}{\partial Y}-1=\theta=0, \quad \text{at } X=0\\
&\psi = \frac{\partial \psi}{\partial Y}=\omega+\frac{\partial^2 \psi}{\partial Y^2}=0, \quad \text{at } Y=0,\\
&\theta = 1, \quad \text{at } Y=0, \quad \text{for } L_1 \leqslant X \leqslant L_1+L_2\\
&\frac{\partial \theta}{\partial Y}=\gamma\theta, \quad \text{at } Y=0, \quad \text{for } L_1 > X > L_1+L_2\\
&\frac{\partial \psi}{\partial Y}=\psi-1=\omega+\frac{\partial^2 \psi}{\partial Y^2}=\frac{\partial \theta}{\partial Y}+\gamma\theta=0, \quad \text{at } Y=1\\
&\frac{\partial \psi}{\partial X}=\frac{\partial \theta}{\partial X}=\frac{\partial^2 \psi}{\partial Y^2}+\frac{\partial^2 \psi}{\partial X^2}+\omega=0, \quad \text{at } X=L_1+L_2+L_3
\end{aligned} \tag{9}$$

Since vorticity is a scalar in a two-dimensional flow, the number of variables is now reduced to three: ψ, ω and θ. The nondimensional velocity components U, V and the nondimensional pressure P are calculated as $U = \partial\psi/\partial Y$, $V = -\partial\psi/\partial X$ once the stream function has been obtained. The resulting Poisson Equation for P is then

$$\frac{\partial^2 P}{\partial X^2}+\frac{\partial^2 P}{\partial Y^2}=-2\left(\frac{\partial^2 \psi}{\partial X \partial Y}\right)^2+2\frac{\partial^2 \psi}{\partial Y^2}\frac{\partial^2 \psi}{\partial X^2}-Ri\frac{\partial \theta}{\partial X} \tag{10}$$

to be solved with the boundary conditions

$$P(0,Y)=0, \quad \left.\frac{\partial P}{\partial X}\right|_{Y=\pm 1}=\frac{1}{Re}\left.\frac{\partial^3 \psi}{\partial Y^3}\right|_{Y=\pm 1}+Ri\theta(X,\pm 1) \tag{11}$$

and the corresponding initial conditions. The main goal of the present work is to obtain the heat flux from the heated surface, which in nondimensional form is given by the local Nusselt number

$$Nu(X,\tau)=\frac{q(x,t)h}{(T_w-T_0)\lambda}=-\left.\frac{\partial\theta}{\partial Y}\right|_{Y=0},\quad \text{for } L_1\leqslant X\leqslant L_1+L_2 \tag{12}$$

The space averaged Nusselt number is then computed by integrating the local Nusselt number along the plate

$$\overline{Nu}(\tau)=\frac{1}{L_2}\int_{L_1}^{L_1+L_2}Nu(X,\tau)\mathrm{d}X. \tag{13}$$

The system of nonlinear equations (6)–(8) along with its boundary conditions is solved by a numerical method based on finite differences, to be described in the next section.

3. Numerical solution procedure

Since the flow governed by Eqs. (6)–(8) is known to be elliptic in space and parabolic in time, iterative procedures must be used and the solution for the problem can only be obtained marching in time. The governing equations along with the boundary conditions are solved numerically by a predictor–corrector method employing finite-difference techniques. In each time step of the predictor–corrector method, the predictor supplies an initial guess for the next time-step solution value employing upwind differencing. The corrector method is then used to improve the initial guess using rearward differencing. The iterative procedure is the following. Using Eq. (7), predicted values for the vorticity ω are obtained at a nondimensional time $\tau+1/2\Delta\tau$. Employing these values of ω, the predicted values for the stream function ψ at $\tau+1/2\Delta\tau$ are obtained using now Eq. (6). The next step is to compute the predicted values of the nondimensional temperature θ for $\tau+1/2\Delta\tau$ after integration of Eq. (8). The corrected values of ω at $\tau+\Delta\tau$ are then calculated using Eq. (7). The final step is to obtain the values of ψ, and θ for $\tau+\Delta\tau$ using the respective equations. The above predictor–corrector approach is carried out for all grid points throughout the channel. In this way, the flow field through the entire channel at time $\tau+\Delta\tau$ is calculated. For numerical stability, positive and negative values of the convective terms in the energy and the vorticity transport equations are discretized with upwind and rearward differencing, respectively, while the buoyancy and diffusion terms are discretized with a central difference formulation. Computations were carried out in an Itanium 2 dual mainframe computer with a 1.6 Ghz processor and a 16 Gb ram memory. All calculations were performed using water ($Pr=7$) as the cooling agent, and wall vorticities were evaluated using the classical Thom's first-order formula [17]

$$\omega_w=\frac{2(\psi_{w+1}-\psi_w)}{\Delta n^2} \tag{14}$$

where Δn is the grid space normal to the wall. Higher order evaluations were not used because it is known that they not always lead to stable solutions [18]. The integration time-step size in this numerical code was adjusted from stability and accuracy criteria with the initial time step size given as an input. In order to avoid numerical errors due to the highly irregular unsteady results, three time-steps of 0.005, 10^{-3}, and 10^{-4} were chosen to test the time-step size sensitivity and convergence of the computations. Results were compared showing that in order to overcome the difficulty of numerical instability, the time increment Δt could be set as 10^{-3} for the flow and heat transfer calculation. This value was chosen because the numerical results for all of the cases studied did not show any noticeable difference in the value of the average Nusselt number when smaller values were used.

In order to get better accuracy at lower cost, a strongly non-uniform staggered grid system with a denser clustering near the heated plate was necessary. Using the boundary layer concepts [19], the computational domain was discretized using coordinate transformation functions to generate a variable grid size system that is closely spaced near the walls of the channel and that gradually becomes coarse away from the heated slab. For the transverse direction a coordinate transformation function $\eta(Y)$ has been employed, obtained from the solution of the following differential equation:

$$\varepsilon^2\frac{\mathrm{d}^2\varphi}{\mathrm{d}s^2}=\varphi-m_y s \tag{15}$$

with the boundary conditions $\varphi(-1/2)=-1/2$ and $\varphi(1/2)=1/2$. This differential equation is known to have two boundary layers at $s=-1/2$ and $s=1/2$. Here, ε is the resulting boundary layer thickness and it is assumed to be very small compared with unity, while m_Y is the slope outside the boundary layer and is therefore positive and very small compared with unity. The solution to Eq. (15) is given by

$$\varphi=m_y s+\frac{(1-m_y)}{2}\frac{\sinh(s/\varepsilon)}{\sinh(1/2\varepsilon)} \tag{16}$$

Substitution of φ by $2\eta-1$ and s by $2Y-1$, gives the desired function as

$$\eta(Y)=\frac{1}{2}+m_y\left(Y-\frac{1}{2}\right)+\frac{(1-m_y)}{2}\frac{\sinh[k_y(Y-1/2)]}{\sinh[k_y/2]} \tag{17}$$

where $k_y=1/\varepsilon$ and must be large compared with unity. The chosen packing parameters of the mesh m_y and k_y, were $m_y=0.4$ and $k_y=10$.

For the longitudinal direction, the coordinate transformation function $\xi(X)$ was found after solving the following differential equation, known to have a boundary layer at $s=0$ (internal boundary layer)

$$\frac{\varepsilon^2}{2}\frac{\mathrm{d}^2\varphi}{\mathrm{d}s^2}+s\left(\frac{\mathrm{d}\varphi}{\mathrm{d}s}-m_x\right)=0 \tag{18}$$

where ε is a small number compared with unity that corresponds to the boundary layer thickness and m_x is the slope outside of the boundary layer. The boundary conditions are $\varphi(0)=0$ and $\varphi(1/2)=1/2$. The solution can be readily obtained as

$$\varphi=m_x s+\frac{1-m_x}{2}\frac{\mathrm{erf}(s/\varepsilon)}{\mathrm{erf}(1/2\varepsilon)} \tag{19}$$

After substituting φ by $\xi-1/2$ and s by $X/(L_1+L_2+L_3)-1/2$, the function $\xi(X)$ is obtained as

$$\xi(X)=\frac{1}{2}+m_x\left(\frac{X}{L_1+L_2+L_3}-\frac{1}{2}\right)+\frac{(1-m_x)}{2}\frac{\mathrm{erf}\left[k_x\left(\frac{X}{L_1+L_2+L_3}-\frac{1}{2}\right)\right]}{\mathrm{erf}[k_x/2]} \tag{20}$$

where $k_x=1/\varepsilon$. The chosen values for the packing parameters in the longitudinal direction were $m_x=0.8$ and $k_x=2$. For the solution of the system of equations, even grid spacing was used in $\xi(X)$ and $\eta(Y)$, generating the desired mesh in the original coordinates X and Y.

The following geometrical values were chosen: $L_1=L_3=3.5$ $(L=8)$ for $Re=100, L_1=L_3=4.5$ $(L=10)$ for $Re=300$ and $L_1=6.5, L_3=4.5$ $(L=12)$ for $Re=500$. In all of the cases studied, the length of the heated slab remained fixed with length $L_2=1$. In order to determine the appropriate grid size, a grid independence study was conducted using four different grid sizes of $131\times81, 121\times71, 111\times61$, and 101×51. It was observed that a further refinement of grids from 101×51 to 131×81 did not have a significant effect on the results in terms of average Nusselt number and the maximum value of the stream function. Based on this observation, a non uniform grid of 101×51 points has been employed for a Reynolds number of 300 and 500. Similar grid dependency studies were carried out for a Reynolds number of 100, and an optimum grid size of 71×51 was obtained. Fig. 2

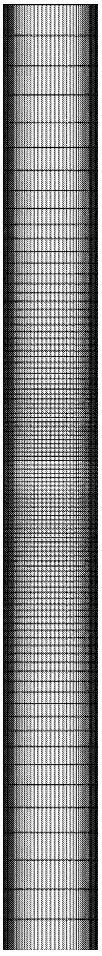

Fig. 2. Mesh employed for a Reynolds number of 300 with a grid size of 101×51 points.

shows the mesh employed for a Reynolds number of 300 with a total of 101×51 grid points.

4. Numerical results

At $\tau = 0$, the downflow produces boundary layer flows close to the surfaces. The space averaged Nusselt number is, using the boundary layer formulation,

$$\overline{Nu}_0 = \frac{1}{L_2}\sqrt{\frac{\overline{Re}}{L_1}}Pr^{1/3}C\left[\left(\frac{L_1+L_2}{L_1}\right)^{3/4}-1\right]^{2/3}$$

with C of order unity. After switching buoyancy on and for relatively large values of the Richardson number, the flow reverses close to the heated plate and the Nusselt number $\overline{Nu}$ first decreases reaching a minimum and then increases again due to the strong upward flow. A vortex develops and the heated fluid reaches the maximum position, represented by a stagnation point at $X = X_s(\tau)$ with the maximum value of X, where $U(X_s, Y) \geqslant 0$ for all Y. It is to be noticed that this point is not a true stagnation point, because the transverse velocity component does not vanish at this point. As the heated column increases, buoyancy forces are larger and the heated fluid climbs and reaches the final position, which is strongly dependent on the Reynolds and Richardson numbers. This climbing process can be smooth or oscillating. Simulations show that when buoyancy forces are relatively small for a given Reynolds number, the location of the stagnation point is fixed. These results are in perfect agreement with the values of the buoyancy parameter that dictate whether the heat transfer regime is steady or oscillatory. As the value of the Richardson (Grashof) number increases, the stagnation point shifts from the upper part of the heated plate to higher regions of the channel. By further increasing the value of the buoyancy parameter, the stagnation point shifts to higher regions of the channel presenting longitudinal oscillations. In general, the values of the Richardson (Grashof) numbers that dictate the type of motion displayed by the stagnation point decrease as the Reynolds number increases. For a given Reynolds number and relatively low Richardson numbers, the steady-state condition can be reached after a relatively short transient, of the order of $\tau \sim 10$. As the Richardson or Grashof number increases for a given Reynolds number, the heated fluid reaches higher altitudes with a longer transient towards the steady-state. Increasing again the Richardson number produces small amplitude flow oscillations in the downstream region of the channel. A further increase of the Richardson number generates larger oscillations which are felt at the upstream regions of the channel. The space averaged Nusselt number also oscillates accordingly.

The numerical results presented in this work correspond in all cases to adiabatic walls with $\gamma = 0$, except when explicitly mentioned. Fig. 3 shows the starting vortex for a Reynolds number of 100, a Richardson number of 8 and a heat loss parameter $\gamma = 0$ (adiabatic channel walls). The elapsed time between frames is $\Delta\tau = 0.2$. The shown images correspond to the zone of the channel where the heated plate is located and the gravity vector is pointing down. The first image Fig. 3a shows the initial streamlines (velocity vectors) and temperature distributions as gray zones. The flow direction reverses and the flow close to the heated slab rises due to buoyancy forces as shown in Fig. 3b. A stagnation region appears above the heated slab. Upward flow is enhanced and the stagnation region shifts to higher portions of the channel. A clockwise recirculation pattern is created as shown in Fig. 3c. The vortex formation increases in size and strength. The vortex center is located in the upper part of the heated plate and Kelvin–Helmoltz instabilities are displayed by the velocity and temperature fields (Fig. 3d). The gradual increment in the vortex size interacts with the forced flow in the central part of the channel. As a result, as shown by Fig. 3e, the lower part of the vortex formation breaks up and casts down while a new recirculation pattern is created. The last image in this figure, Fig. 3f shows the velocity and temperature fields which resemble the cat eyes in the typical Kelvin–Helmoltz instability. As the whole column is filled with hot fluid, buoyancy increases and pushes the vortex upwards. For any given value of the Reynolds number and relatively low values of the Richardson (Grashof) number, the transient response leads to a steady-state solution as shown for the streamlines (left) and isotherms (right) in Fig. 4, for a Reynolds number of 100 and three different values of the Richardson number. Instead of using the longitudinal coordinate, the hight is employed as $8 - X_s$. A well-steady rotating clockwise vortex structure is formed with increasing size as the Richardson number increases. As the Richardson number increases, the single vortex structure changes to a swinging vortex train with strong transverse oscillations with increasing amplitudes in the downstream region. Fig. 5 shows the transient streamlines and isotherms for the case of $Re = 300$ and $Ri = 5$, at three different times. A two or three vortex structure develops with time coexisting with small counter clockwise rotating vortices close to the wall. For these parameters, an oscillatory solution is obtained without any steady final response. Therefore, in order to follow the migration of the vortex structure, the value of the stagnation point X_s is plotted as a function of time for three different values of the Reynolds numbers in Figs. 6–8, as functions of the nondimensional time with selected values of the Richardson number. For small Reynolds and Richardson numbers flow (as for example $Re = 100$ and $Ri < 5$ in

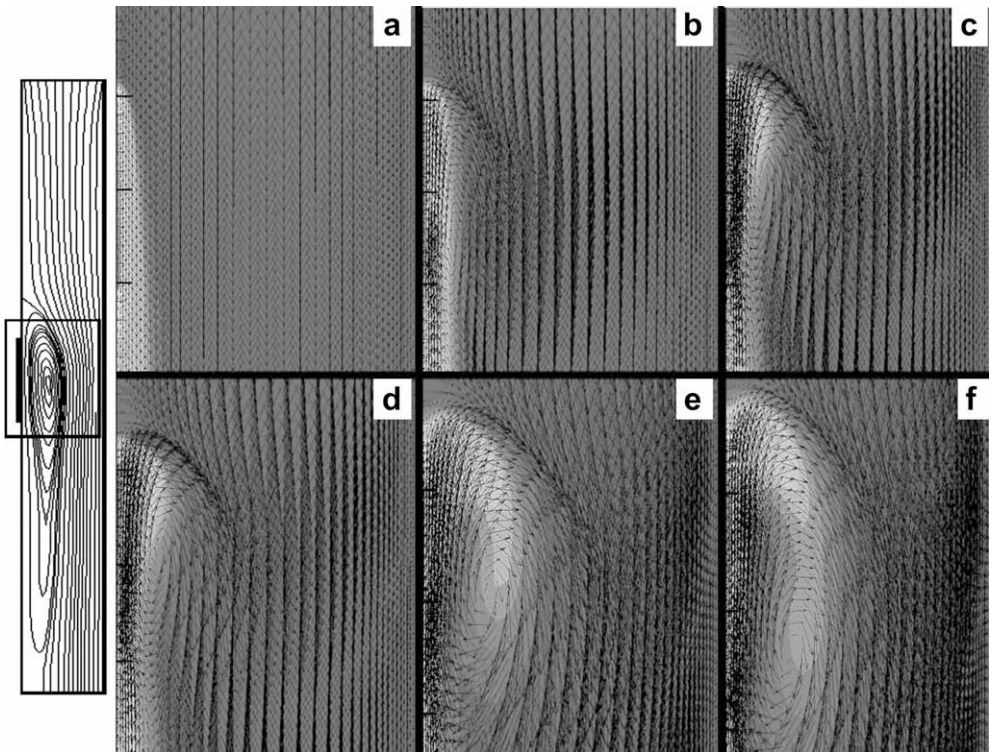

Fig. 3. Vortex formation for $Re = 100$ and $Ri = 8$. The displayed images correspond to the channel section shown with nondimensional time intervals of 0.2.

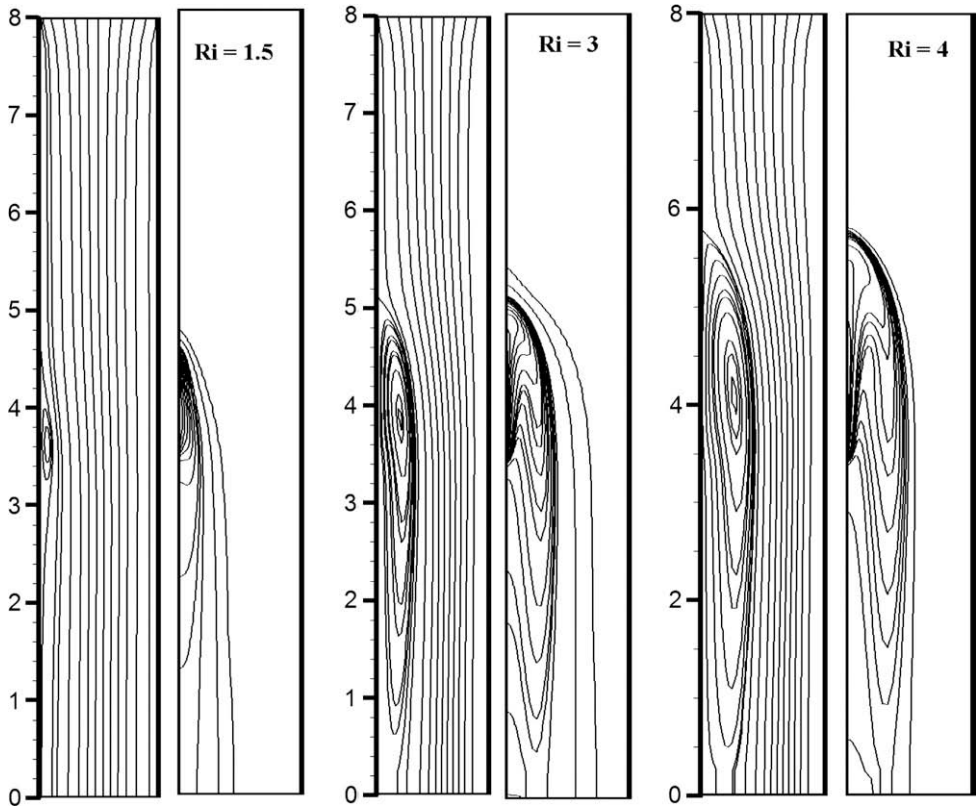

Fig. 4. Steady streamlines and isotherms for a Reynolds number of 100 for different values of the Richardson number.

Fig. 6), the vortex formation and migration is smooth, reaching the final steady-state only after a nondimensional induction time which increases with the Richardson number. However, for larger Richardson number flows, the transient process leading to the final vortex upstream position is not more smooth, but occurs after some jumps and/or oscillations. This latter behavior can be observed in Fig. 6 for a $Re = 100$ and $Ri = 8$, and in Fig. 7 for a $Re = 300$ and $Ri = 5$.

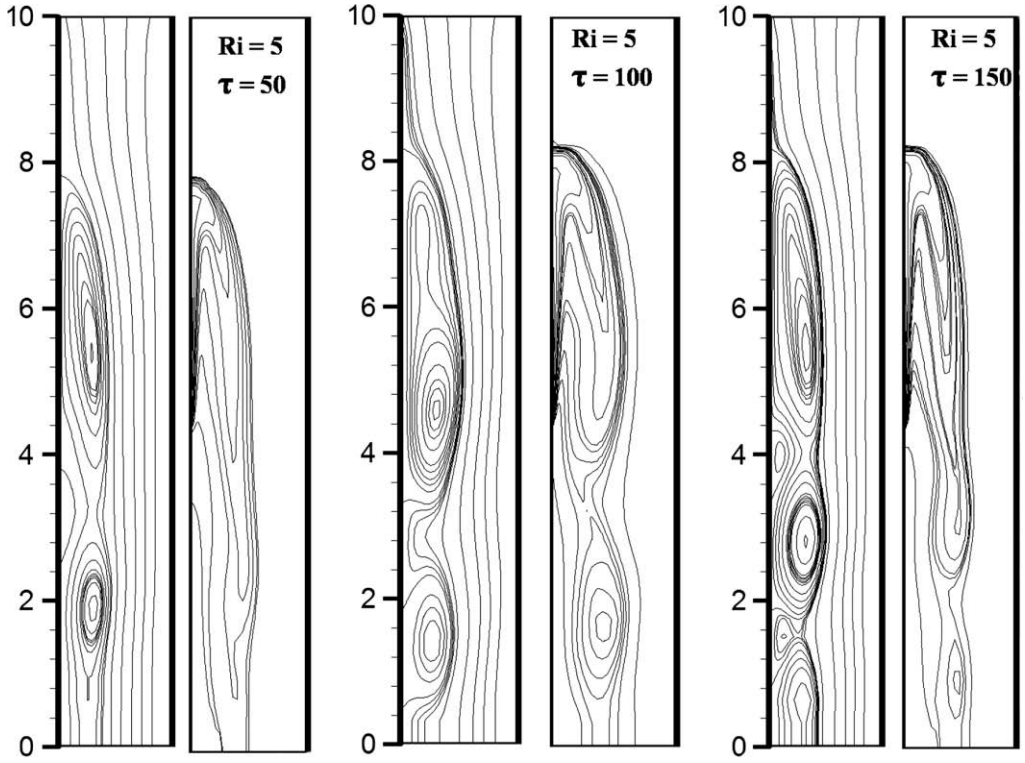

Fig. 5. Transient streamlines and isotherms for a Reynolds number of 300 and a Richardson number of $Ri = 5$ ($Gr = 4.5 \times 10^5$).

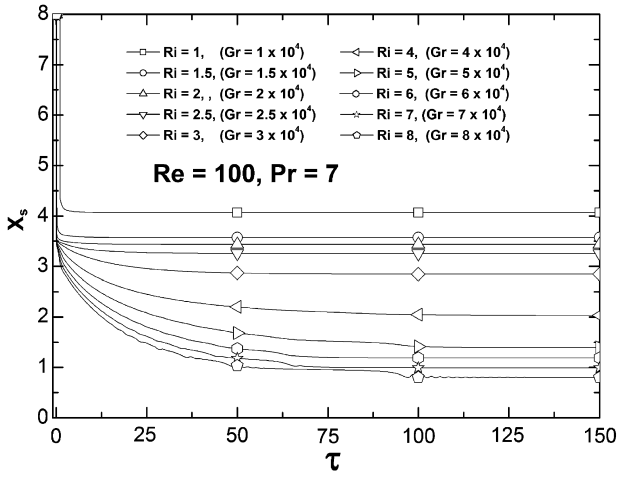

Fig. 6. Location of the stagnation point for a Reynolds number of $Re = 100$ and $Pr = 7$.

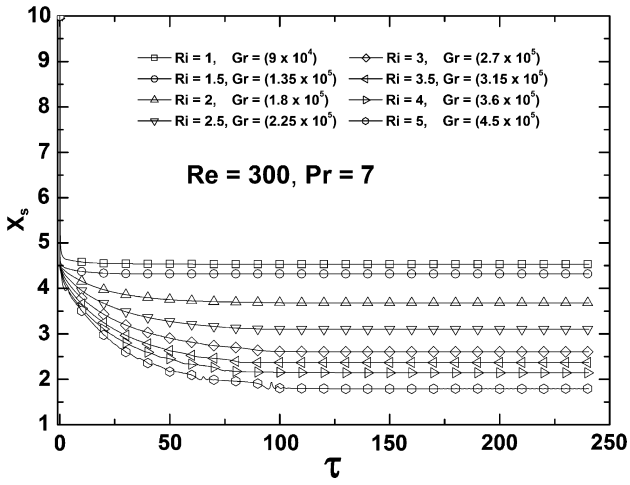

Fig. 7. Location of the stagnation point for a Reynolds number of $Re = 300$ and $Pr = 7$.

Figs. 9–11 show the influence of the buoyancy parameter in the longitudinal velocity component. The images displayed show typical instantaneous longitudinal velocity profiles throughout the whole channel length. In this case, forced flow has an upward direction and reversed flow has the opposite direction due to the differential heating which is located at the left side of the instantaneous velocity profiles. In Fig. 9–11, the images at the upper left corner correspond to the initial velocity profile for $\tau = 0$, and they illustrate the influence of the Reynolds number in the flow development. The images displayed show that when the buoyancy parameter increases, flow reversal is enhanced and the maximum longitudinal velocity value of the forced flow also increases. Fig. 9 shows the instantaneous velocity profiles for a Reynolds number of 100 and three different values of the Richardson (Grashof) number: $Ri = 3$ ($Gr = 3 \times 10^4$), 6 ($Gr = 6 \times 10^4$), and 8 ($Gr = 8 \times 10^4$). Fig. 10 shows the instantaneous velocity profiles for a Reynolds number of 300 and three different values of the Richardson (Grashof) numbers: $Ri = 1$ ($Gr = 9 \times 10^4$), 3 ($Gr = 2.7 \times 10^5$), and 5 ($Gr = 4.5 \times 10^5$). Fluctuations in the resultant flow are increased due to the oscillations presented by the main vortex formation due to an increase in the buoyancy parameter. Fig. 11 shows the instantaneous velocity profiles for a Reynolds number of 500 and three different values of the Richardson (Grashof) numbers: $Ri = 1$ ($Gr = 2.5 \times 10^5$), 2 ($Gr = 5 \times 10^5$), and 3 ($Gr = 7.5 \times 10^5$). Figs. 9–11 illustrate how the resulting flow in the channel becomes more sensitive to buoyancy forces as the Reynolds number is increased, resulting in an enhancement of flow reversion.

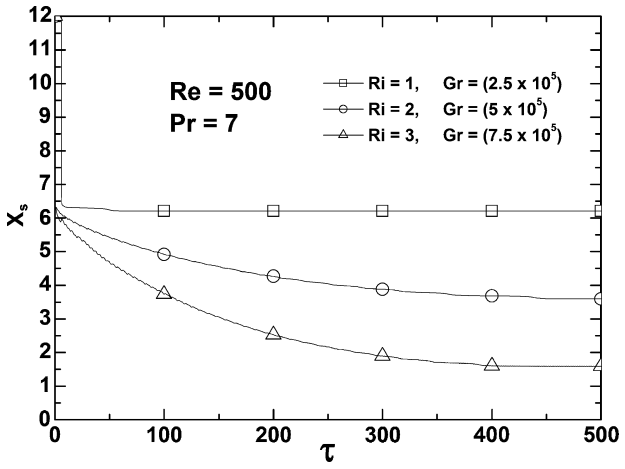

Fig. 8. Location of the stagnation point for a Reynolds number of $Re = 500$ and $Pr = 7$.

In order to represent the transient process and the flow oscillations in a simple way, a single parameter which characterizes the flow response Y_p is introduced as the first moment of the longitudinal velocity component (mass flux centroid)

$$Y_p(X_0,\tau) = \frac{1}{\overline{U}}\int_0^1 U(X_0,Y,\tau)Y\,dY = \int_0^1 U(X_0,Y,\tau)Y\,dY \qquad (21)$$

where $\overline{U}$ corresponds to the average velocity in the selected position X_0, $\overline{U} = \int_0^1 U\,dY = 1$. To obtain the mass flux centroid, the region that corresponds to the channel's midsection was employed first as the reference region, $X_0 = L_1^* + 0.5L_2^*$. The time variations of the mass flux centroid are directly related to the transverse flow oscillations. Figs. 12–15 illustrate the mass flux oscillations as a function of the nondimensional time for three different values of the Reynolds number, 100, 300, and 500, for different ranges of the buoyancy parameter. Fig. 12 shows that for a Reynolds number of 100, transversal oscillations felt at the channel's midsection are practically non-existent for the Richardson numbers plotted of $Ri \leqslant 8$, for large nondimensional times. However, in the long transient towards the final steady-state, transversal flow oscillation appeared for relatively large values of the Richardson numbers, larger than 4. The oscillations for $Ri = 8$, have a clear nondimensional frequency or Strouhal number of $St = fh/u_0 = 0.43$. For the highest value of the buoyancy parameter used in this figure, $Ri = 8$, the flow reaches the final steady state condition only after $\tau \sim 140$. For a Reynolds number of $Re = 300$, Fig. 13 shows how the transverse oscillations are considerably more intense in comparison with the previous Reynolds number. For small values of the buoyancy parameter $Ri < 4$, $(Gr < 5.44 \times 10^5)$, transverse oscillations are small in amplitude and are quickly damped. For higher values of the buoyancy parameter, the amplitude of the transverse oscillations increased dramatically and the final solution seemed to be oscillatory. Fig. 14 shows the normalized power spectrum of the flow oscillation for a Richardson number of $Ri = 5$, showing clearly the peak at the corresponding Strouhal number of $St = 0.52$. Fig. 15 shows how for a Reynolds number of $Re = 500$ and $Ri \geqslant 2$, the mass flux centroid is located very close to the right wall of the channel. For $Ri = 1$, a final steady-state is achieved after a relatively short transient. However, for $Ri \geqslant 2$, strong flow oscillations occur, with larger amplitude as the Richardson number increases. Fig. 16 shows the normalized power spectrum for a $Ri = 3$, showing a couple of important peaks ranging from 0.1 to 0.5 in the Strouhal numbers.

In order to illustrate the way in which the intensity of the transverse oscillations in the flow vary at the selected position X_0, mass flux centroides were obtained at several positions of the channel. Figs. 17–19 show how the amplitude of the transverse oscillations increase in the downstream direction. Fig. 17 shows the mass flow

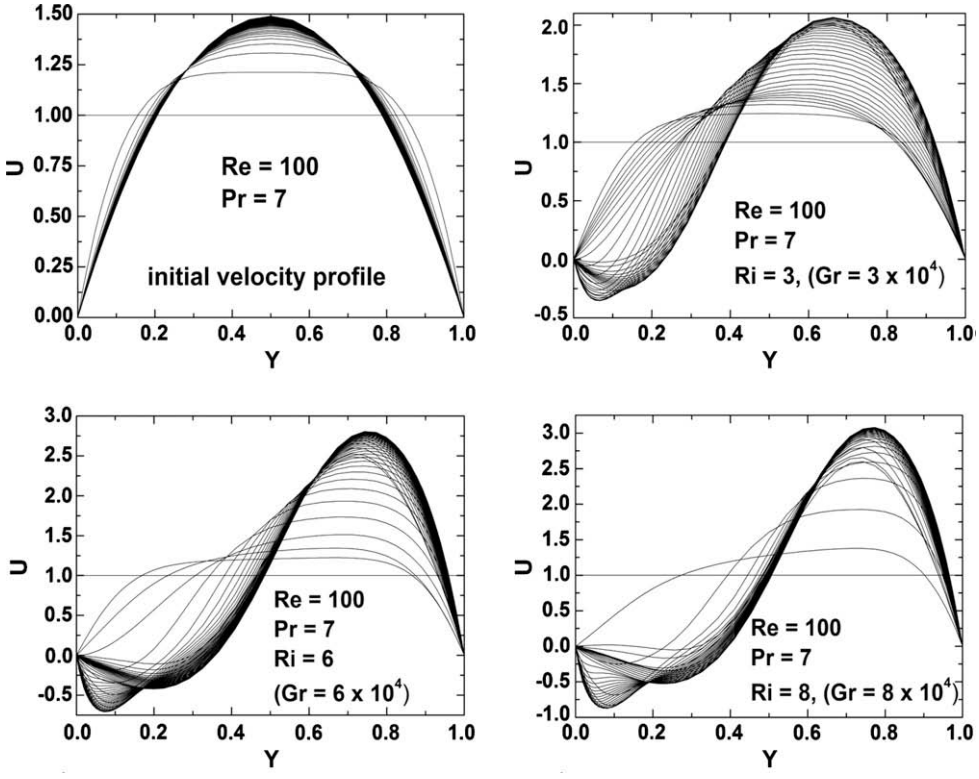

Fig. 9. Velocity profiles for a Reynolds number of 100.

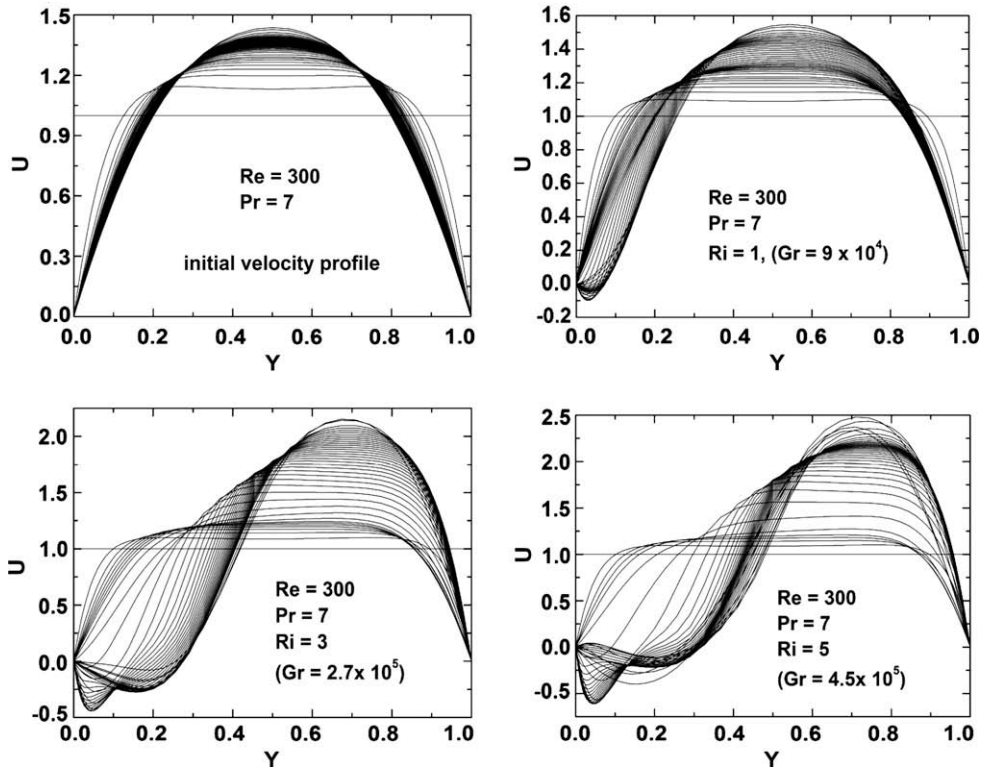

Fig. 10. Velocity profiles for a Reynolds number of 300.

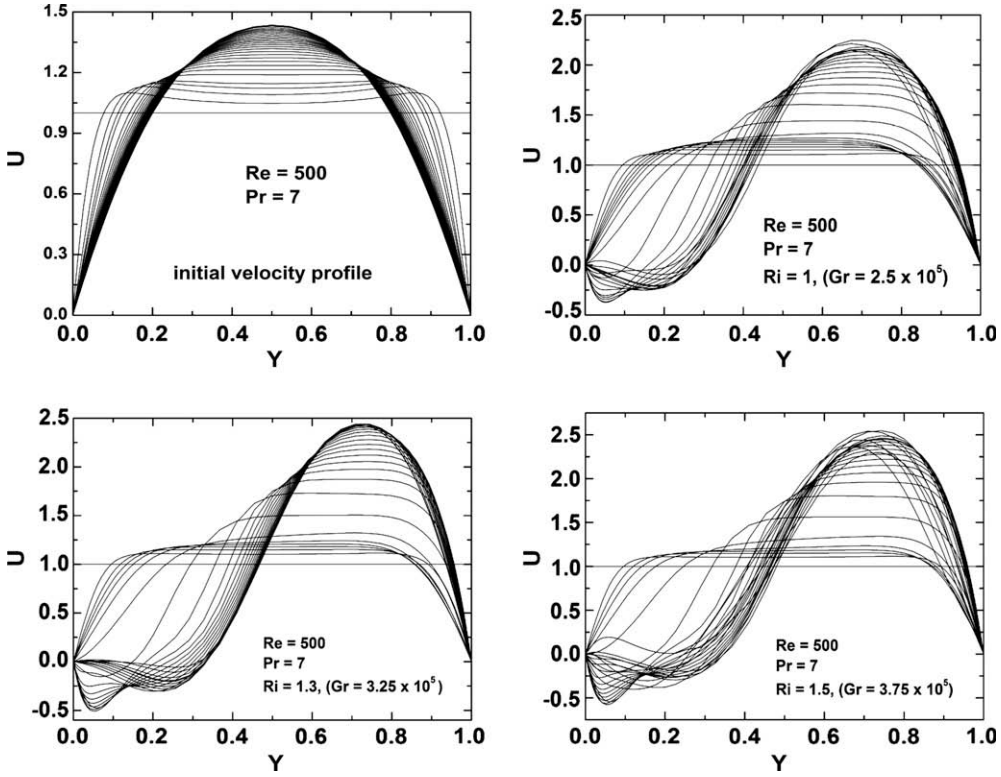

Fig. 11. Velocity profiles for a Reynolds number of 500.

centroides for a Reynolds number flow of 300, a Richardson number of 2 and a nondimensional channel length of $L = 10$, that is for the parametric set [300, 2, 10]. There is a smooth transition to the final steady state without any flow oscillation in the whole channel. The mass flow centroid increases continuously downstream. Fig. 18 shows the same variable for the parametric set [300, 3.5,

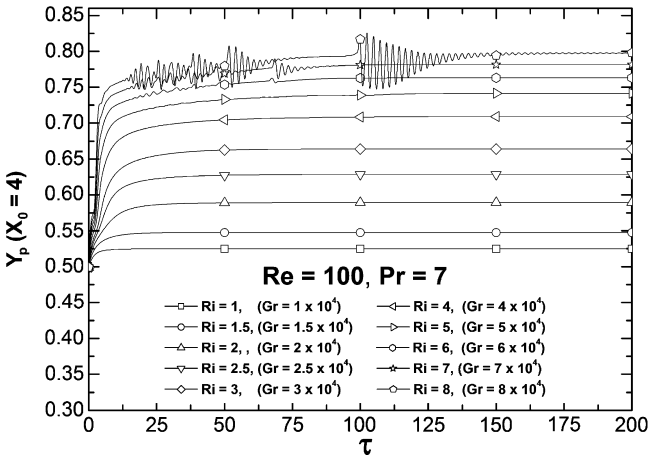

Fig. 12. Location of the mass flux centroid for a Reynolds number of $Re = 100$ at the channel's midsection.

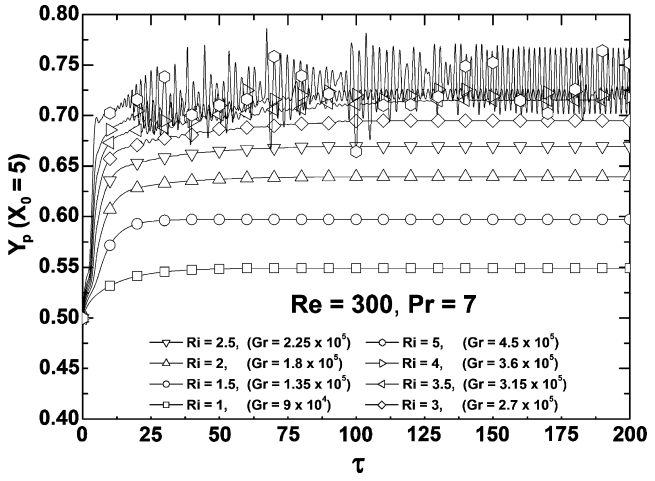

Fig. 13. Location of the mass flux centroid for a Reynolds number of $Re = 300$ at the channel's midsection.

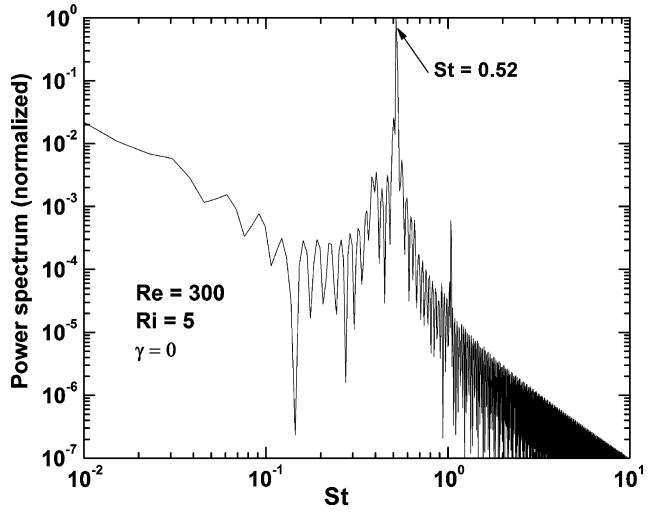

Fig. 14. Strouhal number of the mass flux oscillations for a Reynolds number of 300 and $Ri = 5$ ($Gr = 4.5 \times 10^5$).

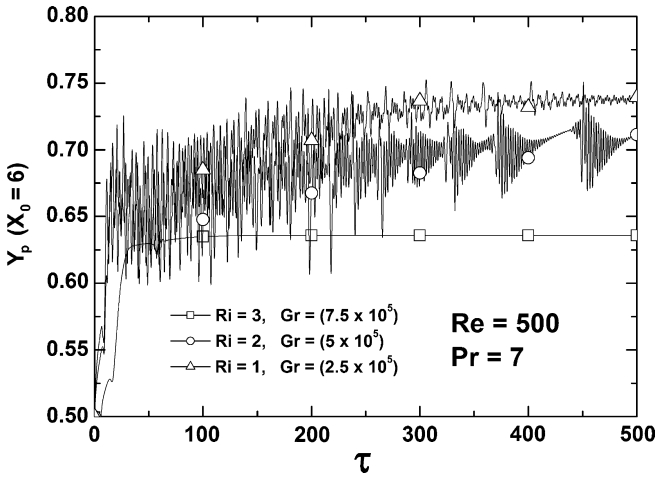

Fig. 15. Location of the mass flux centroid for a Reynolds number of $Re = 500$ at the channel's midsection.

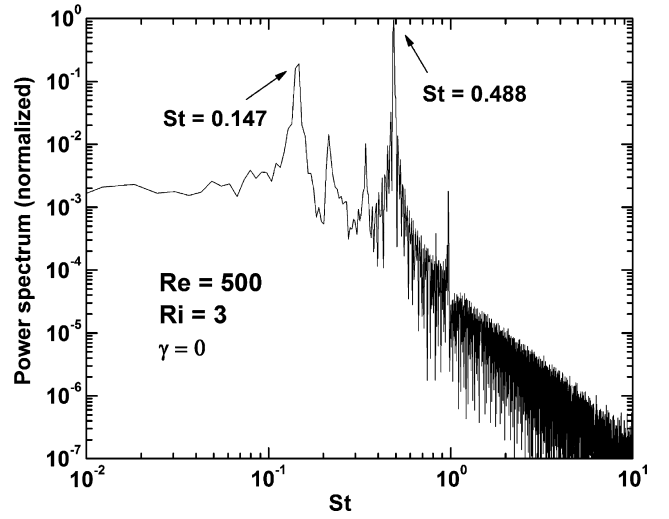

Fig. 16. Strouhal number of the mass flux oscillations for a Reynolds number of 500 and $Ri = 3$ ($Gr = 7.5 \times 10^5$).

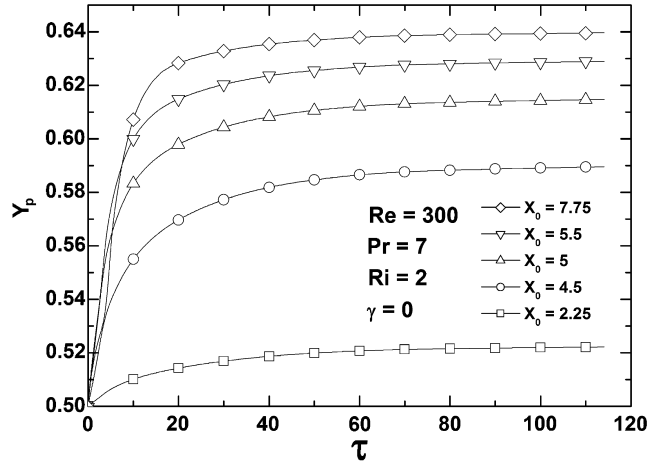

Fig. 17. Mass flux centroid throughout the whole channel length for $Re = 300$ and $Ri = 2$ ($Gr = 1.8 \times 10^5$).

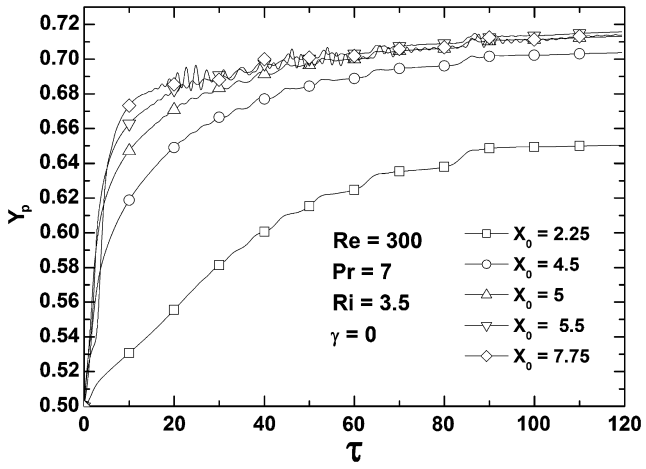

Fig. 18. Mass flux centroid throughout the whole channel length for $Re = 300$ and $Ri = 3.5$ ($Gr = 3.15 \times 10^5$).

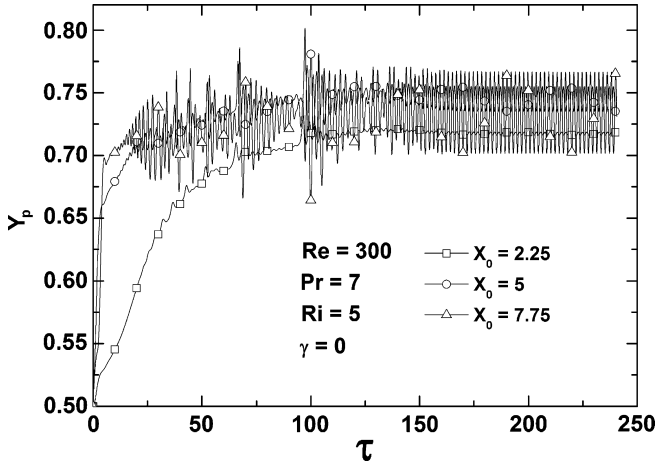

Fig. 19. Mass flux centroid throughout the whole channel length for $Re = 300$ and $Ri = 5$ ($Gr = 4.5 \times 10^5$).

10]. The flow structure now becomes more homogenous in the downstream regions of the channel. In this figure, some jumping processes are evident and small amplitude flow oscillations appeared at the downstream position of the channel. Fig. 19 shows the mass flux centroides for the parametric set [300, 5, 10]. Here, strong flow oscillations arise almost in the whole channel, except in the most upstream position. The amplitude of the flow oscillations increase dramatically in the downstream region of the channel. The oscillations are not present in the upper part of the channel, which corresponds to positions close to the final stagnation point ($X < X_s$), with $X_s \simeq 1.7$. However, the mass flux centroid moves to the right in the upper part of the channel ($X_0 = 2.5$) but without remarkable oscillations, indicating that the produced vortex structure influences the flow almost in the whole channel. The mean maximum value of the mass flux centroides occurs at the middle of the channel, $X = 5$. The resulting flow oscillations seem to be sustained up to the final nondimensional computing time of 250, indicating that a Hopf bifurcation takes place.

5. Heat transfer

In this section, results for the temporal variations in the averaged Nusselt number, $\overline{Nu}(\tau)$ are presented. Computation is started immediately after the sudden imposition of gravity at $\tau = 0$, and

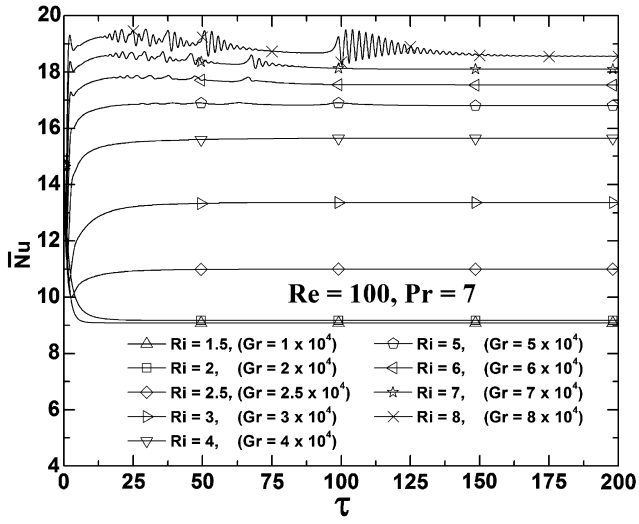

Fig. 20. Averaged Nusselt number in the heated plate for a Reynolds number of $Re = 100$ and $Pr = 7$.

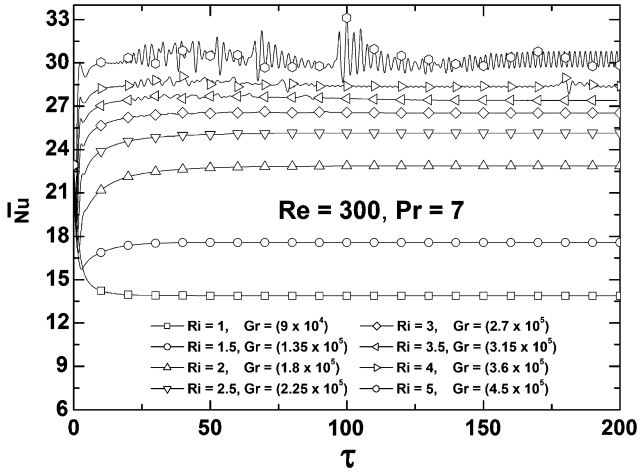

Fig. 21. Averaged Nusselt number in the heated plate for a Reynolds number of $Re = 300$ and $Pr = 7$.

simulations were carried out until the averaged Nusselt number reached steady state or clearly showed a final oscillatory behavior. Fig. 20 shows the predicted temporal evolution on the averaged Nusselt number for a Reynolds number of 100 for several values of the buoyancy parameter. The flow and heat transfer finally reached the steady-state condition. The transient nondimensional time needed to reach the final steady-state increases with increasing Richardson (Grashof) numbers. At low opposing buoyancy Richardson numbers, $Ri < 4$ ($Gr < 4 \times 10^4$), steady state is reached at $\tau \sim 30$. As the buoyancy parameter is further increased, the duration of the transient before reaching steady state also increases, and oscillations appeared in the transient response. Fig. 20 shows how for a value of the buoyancy parameter of $Ri = 8$ ($Gr = 8 \times 10^4$), steady state is reached at $\tau \sim 150$. Fig. 21 shows the averaged Nusselt number for a Reynolds number of $Re = 300$ and illustrates how heat transfer is enhanced by increasing the value of the buoyancy parameter. Simulations were carried out up to $\tau = 250$. Results show that with this higher Reynolds number, a stronger reverse flow appears earlier. This figure illustrates how buoyancy forces have become more sensitive with an increase in the Reynolds number. Oscillation and periodicity is

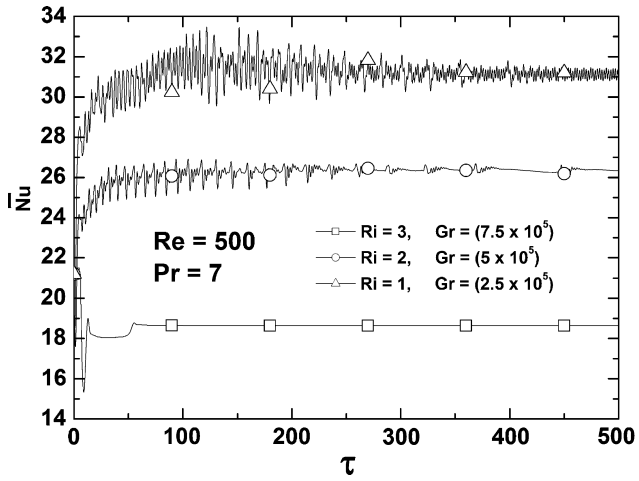

Fig. 22. Averaged Nusselt number in the heated plate for a Reynolds number of $Re = 500$ and $Pr = 7$.

exhibited by the averaged Nusselt number for relatively large Richardson numbers such as $Ri = 5$. For a Richardson number of $Ri = 4$, small imperceptible oscillations arise. However, for a Richardson number of $Ri = 5$ the averaged Nusselt number oscillates, with an almost constant frequency $(St = 0.52)$ for nondimensional times larger than $\tau = 150$. In Fig. 22, for a Reynolds number of $Re = 500$, the values of the Richardson (Grashof) number for steady and transition to oscillatory heat transfer are further reduced. The fluctuating flow and thermal response clearly indicate that under the strong action of the opposing buoyancy, the flow has become rather unstable. A final steady-state is reached for a Richardson number of $Ri = 1$, although the transient is not smooth. For a Richardson number of $Ri = 2$, the transient process contains oscillation windows with decreasing frequency as time increases. The final nondimensional time used in the computations $(\tau = 500)$ does not show that for this Richardson number a final steady state can be reached. For higher Richardson numbers, an oscillatory averaged Nusselt number is obtained with complex power spectra.

5.1. Non-adiabatic channel walls

In this section the influence of the wall heat loss parameter γ is presented using a similar flow configuration as previously reported experimental work [16]. The selected parametric set to be employed in the numerical simulations is [300, 6.7, 6.3]. Fig. 23 shows typical streamlines (left) and isotherms (right) for three different values of the heat loss parameter γ. For adiabatic walls and relatively long times, a three vortex structure is formed covering the whole system and the heated fluid climbs almost to the channel entrance. The imposed boundary condition in the upper part of the channel has a strong influence in the response. For $\gamma = 10$, the heat losses to the wall produce a decrease in the length of the vortex structure as shown in the middle pair of Fig. 23. For very strong wall heat losses $(\gamma = 100)$, the response now produces a very short flow vortical structure, with the boundary conditions corresponding to a wall temperature close to the fluid inlet temperature. Fig. 24 shows the averaged Nusselt numbers for the three cases considered: $\gamma = 0$, 10 and 100. Fig. 24a shows the averaged Nusselt number for the case of adiabatic walls $(\gamma = 0)$. The flow and heat transfer from the heated slab shows a multi-spectral response. In the inset of Fig. 24a only the steady oscillatory behavior is plotted for clarity in a limited range of the nondimensional time, from $\tau = 200$ to $\tau = 250$. However, as the heat losses through the channel walls increase, the flow and heat transfer from the heated slab become more organized and a transition from the multi-spectral to a monospectral behavior is achieved. Fig. 24b shows the case

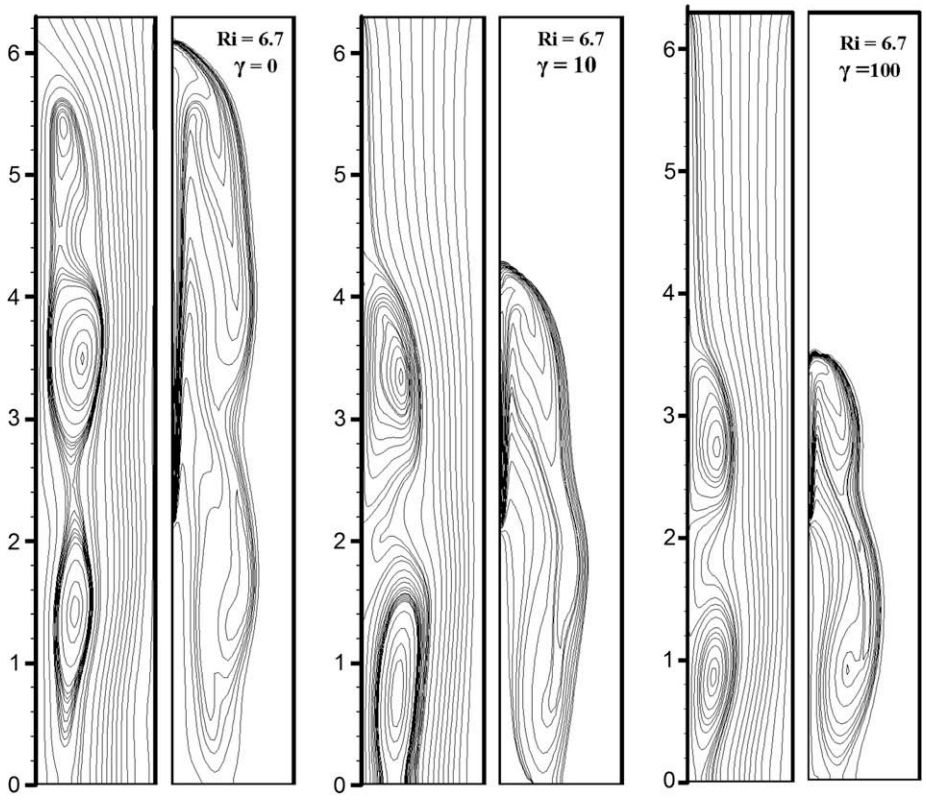

Fig. 23. Streamlines and isotherms for different values of the heat loss parameter γ.

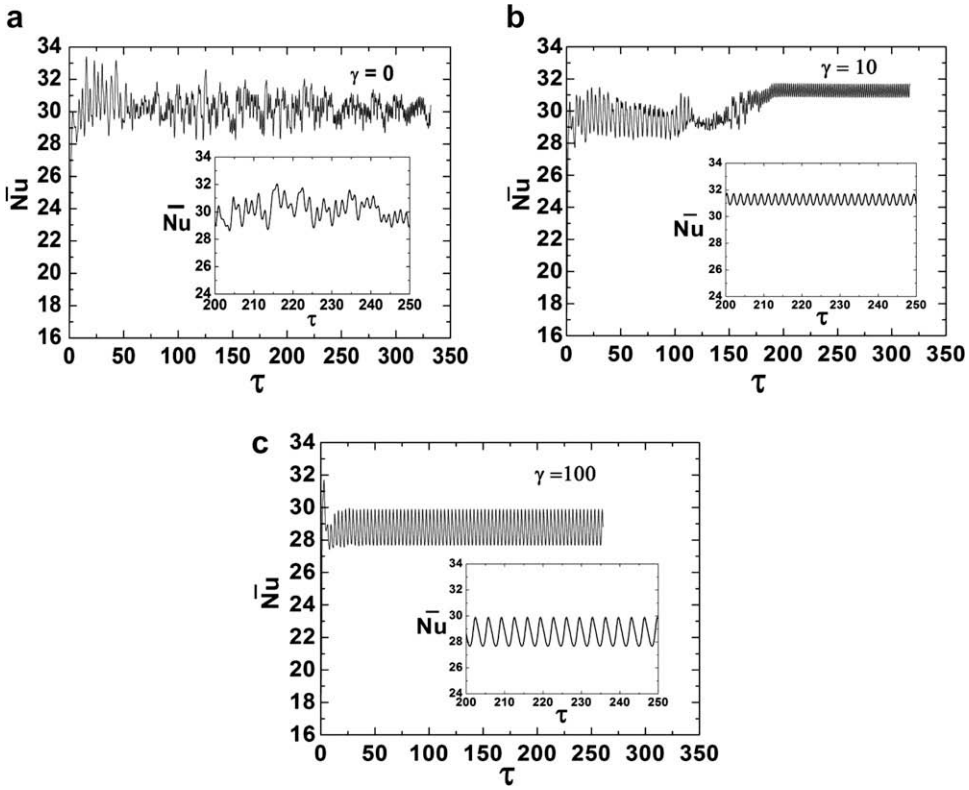

Fig. 24. Averaged Nusselt number for different values of the heat loss parameter γ using the parametric set [300,6.7,6.3].

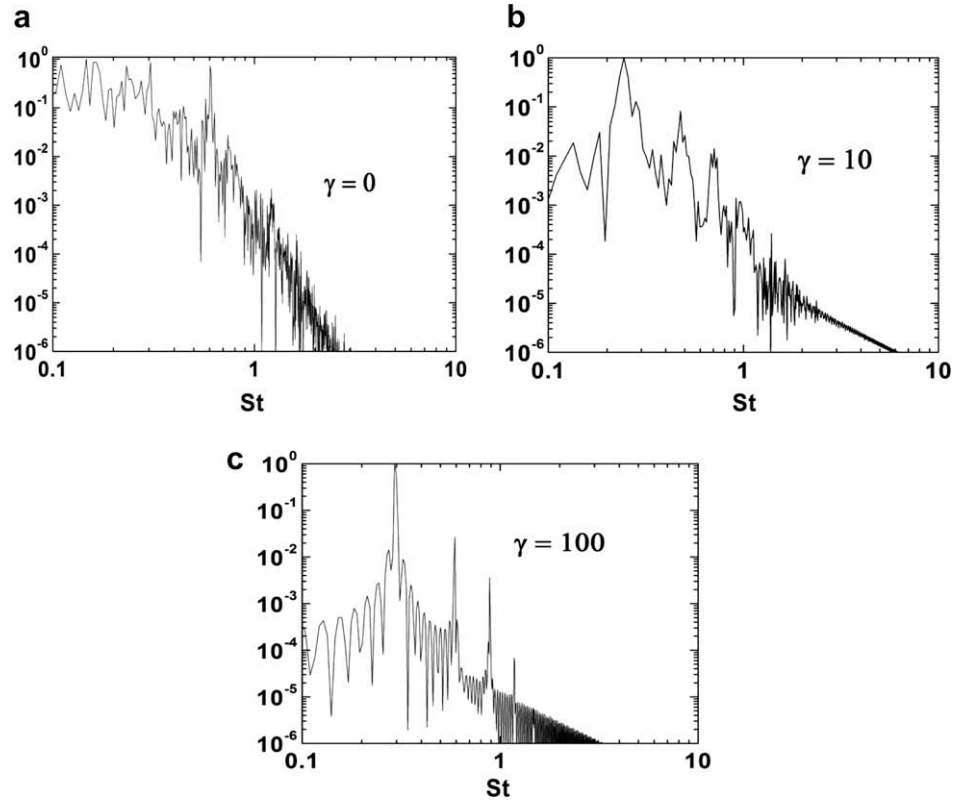

Fig. 25. Normalized power spectra of the mass flux oscillations, for different values of the heat loss parameter γ using the parametric set [300, 6.7, 6.3].

for $\gamma = 10$. After a long transition of $\tau \sim 200$, with a flow response of similar characteristics to the case of adiabatic walls, the flow achieves a more regular harmonic pattern. Fig. 24c shows the case of $\gamma = 100$ (practically corresponding to the case of cold walls), the response is almost harmonic after the initial short transient of $\tau \sim 20$. The normalized power spectra for the averaged Nusselt

number as a function of the Strouhal number are plotted in Fig. 25 for the three cases considered. For adiabatic walls, Fig. 25a shows the multi-spectral response with several peaks, ranging from $St \sim 0.1$ to $St \sim 0.6$. When the wall heat losses increase, only the peak $St \sim 0.28$ survives, as shown in Fig. 25b and c. Fig. 26 shows the mass flux centroid at $X_0 = L_1$ as a function of the nondimensional time for the three cases considered. A similar behavior as with the averaged Nusselt number is obtained, showing a nice harmonic behavior for large values of parameter γ. The experimental results reported in [16] are also shown in Fig. 27. The reported frequency in the experimental work seems to have larger values than the numerical results. The lack of temporal resolution in [16] may be responsible for the discrepancy. The mean mass flux centroid decreases as the heat loss parameter increases. For large values of γ, the mass flux centroid has a mean of $Y_p(X_0 = L_1) \simeq 0.65$ with an amplitude of 0.03. Finally, the final upper stagnation point X_s is plotted in Fig. 28 as a function of the heat loss parameter.

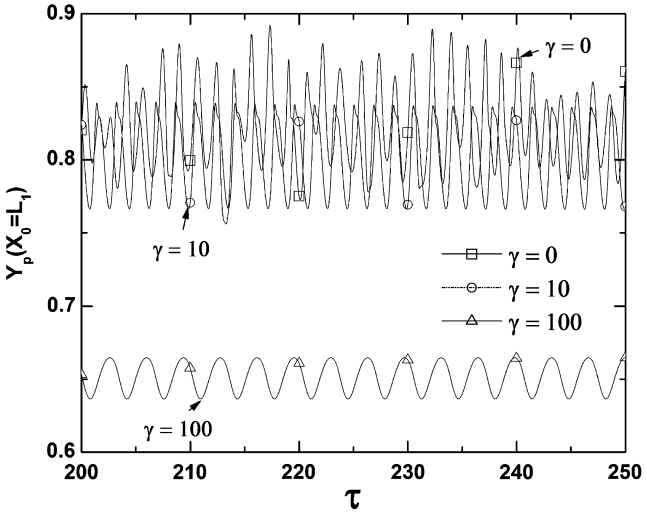

Fig. 26. Mass flux centroid for different values of the heat loss parameter γ using the parametric set [300, 6.7, 6.3].

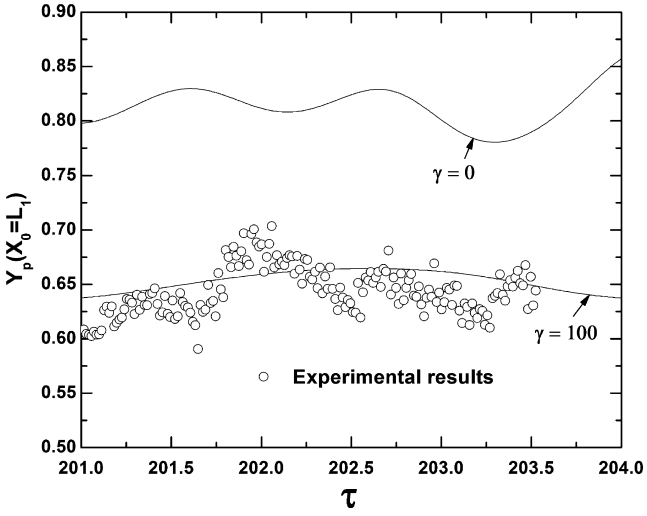

Fig. 27. Experimental and numerical mass flux centroid.

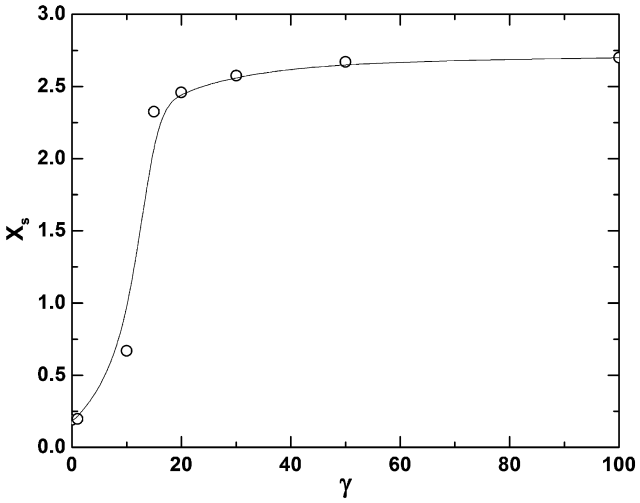

Fig. 28. Location of the final upper stagnation point for different values of the heat loss parameter γ using the parametric set [300, 6.7, 6.3].

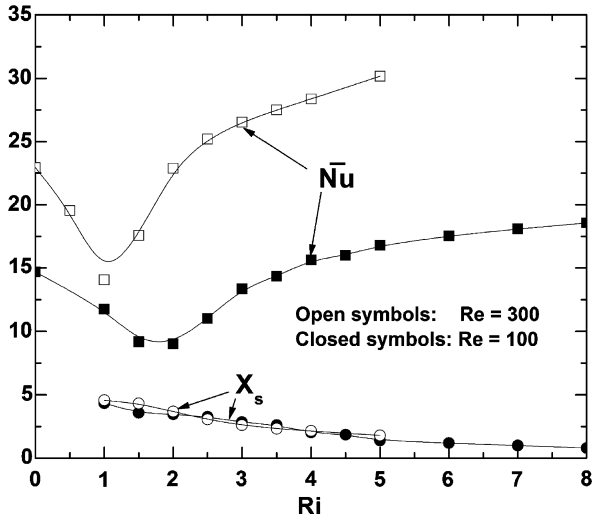

Fig. 29. Final averaged Nusselt number and location of the stagnation point as functions of the Richardson number for $Re = 100$ and 300.

6. Conclusion and remarks

A laminar, two-dimensional and opposing mixed convection flow with a flat velocity distribution at the entrance of a vertical channel with non-adiabatic walls and a discrete and isothermal heat source has been studied numerically. The nondimensional governing equations are solved using a nonuniform spacing in both directions. A parametric study was carried out to evaluate the influence of the buoyancy and inertia effects in the temporal evolution of the velocity and temperature fields along with the plate overall heat transfer. The influence of the Reynolds and Richardson (Grashof) numbers in the transient formation of the vortical structure, the vortex location and the vortex dimensions on the heat transfer are studied. For a given Reynolds number and relatively small value of the Richardson number, the transient process leads to a final steady-state. As buoyancy increases, the heated fluid climbs towards the upper channel entrance, producing a vortical structure with one or several clockwise rotating vortices and strong transverse flow oscillations, with increasing amplitudes in downstream positions. The convection instability occurs as a Hopf

bifurcation with a well defined frequency close to $St \simeq 0.52$. Finally, Fig. 29 shows the final mean space averaged Nusselt number and the location of the stagnation point (upper vortex position) as a function of the Richardson number for $Re = 100$ and $Re = 300$. The Nusselt number first decreases and later increases with the Richardson number. The Richardson number for the minimum averaged Nusselt number decreases with the Reynolds number. The same seems to occur with the critical value of the Richardson number for instability. The position of the upper stagnation point decreases monotonically with the Richardson number and gives a similar profile for both Reynolds numbers. However, it is to be noticed that the channel lengths in both cases are different.

Acknowledgement

This work has been supported by DGAPA of UNAM, under Contract No. IN-1114505.

References

[1] J. Hartnett, M. Kostic, Heat transfer to Newtonian and non-Newtonian fluids in rectangular ducts, Adv. Heat Transfer 19 (1989) 247–356.
[2] W. Aung, G. Worku, Theory of fully developed, combined convection including flow reversal, ASME J. Heat Transfer 108 (1986) 485–488.
[3] W. Aung, G. Worku, Developing flow and flow reversal in a vertical channel with asymmetric wall temperatures, ASME J. Heat Transfer 108 (1986) 299–304.
[4] E.M. Sparrow, G. Chrysler, L. Azevedo, Observed flow reversals and measured-predicted Nusselt numbers for natural convection in a one sided heated vertical channel, J. Heat Mass Transfer 106 (1984) 325–332.
[5] D. Elpidorou, V. Prasad, V. Modi, Convection in a vertical channel with a finite wall heat source, Int. J. Heat Mass Transfer 34 (1991) 573–578.
[6] T. Lin, C.P. Yin, W.M. Yan, Transient laminar mixed convective heat transfer in a vertical flat duct, ASME J. Heat Transfer 113 (1991) 384–390.
[7] T.-F. Lin, T.-S. Chang, Y.-F. Chen, Development of oscillatory asymmetric recirculating flow in transient laminar opposing mixed convection in a symmetrically heated vertical channel, ASME J. Heat Transfer 115 (1993) 342–352.
[8] L.S. Yao, Free and forced convection in the entry region of a heated vertical channel, Int. J. Heat Mass Transfer 26 (1983) 65–72.
[9] T.-S. Chang, T.-F. Lin, Steady and oscillatory opposing mixed convection in a symmetrically heated vertical channel with a low-Prandtl number fluid, Int. J. Heat Mass Transfer 36 (1993) 3783–3795.
[10] Y.-C. Chen, J. Chung, Stability of mixed convection in a differentially heated vertical channel, ASME J. Heat Transfer 120 (1998) 127–132.
[11] C.-H. Cheng, C.-J. Weng, W. Aung, Buoyancy-assisted flow reversal and convective heat transfer in the entrance region of a vertical rectangular duct, Int. J. Heat Fluid Flow 21 (2000) 403–411.
[12] G. Evans, R. Greif, Buoyant instabilities in downward flow in a symmetrically heated vertical channel, Int. J. Heat Mass Transfer 40 (1997) 2419–2430.
[13] C.-H. Cheng, S.-Y. Huang, W. Aung, Numerical predictions of mixed convection and flow separation in a vertical duct with arbitrary cross section, Numer. Heat Transfer, Part A 41 (2002) 491–514.
[14] J.-H. Jang, W.-M. Yan, Mixed convection heat and mass transfer along a vertical wavy surface, Int. J. Heat Mass Transfer 47 (2004) 419–428.
[15] M.S. El-Din, Effect of thermal and mass buoyancy forces on the development of laminar mixed convection between vertical parallel plates with uniform wall heat and mass fluxes, Int. J. Therm. Sci. 42 (2003) 447–453.
[16] L. Martínez-Suástegui, C. Treviño, Particle image velocimetry measurements for opposing flow in a vertical channel with a differential and asymmetric heating condition, Exp. Therm. Fluid Sci. 32 (2007) 262–275.
[17] A. Tom, The flow past circular cylinders at low speeds, Proc. R. Soc. A 141 (1933) 651–669.
[18] D. Anderson, J. Tannehill, R. Pletcher, Computational Fluid Mechanics and Heat Transfer, Taylor & Francis, New York, 1984.
[19] C. Bender, S. Orszag, Advanced Mathematical Methods for Scientists and Engineers, McGraw Hill, New York, 1978.